

A high-efficiency and broadband reflective 90° linear polarization rotator based on anisotropic metamaterial

Jingcheng Zhao¹ · Yongzhi Cheng²

Received: 30 April 2016 / Accepted: 19 September 2016 / Published online: 26 September 2016
© Springer-Verlag Berlin Heidelberg 2016

Abstract In this paper, a high-efficiency and broadband reflective linear polarization rotator based on anisotropic metamaterial is proposed, which is verified by simulation and experiment. Simulated results indicate that our design can achieve 90° polarization rotation from 5.7 to 10.3 GHz with the relative bandwidth of 57.5 %, which is agreement well with experiment. The further simulated results indicate that our design can achieve linear polarization conversion or rotation by 90° under oblique incident angles with large range for both transverse electric and transverse magnetic waves. Finally, the amplitude and phase of reflective coefficients with different polarization, and surface current distribution of the unit cell structure are simulated to explain the physics mechanism of the high-efficiency and broadband polarization rotation. Our design will provide an important reference for the practical applications of the metamaterial in polarization manipulation.

1 Introduction

The polarization refers to the oscillating direction of an electric field in a plane perpendicular to the propagation direction, which is a basic and important property of the electromagnetic (EM) waves or lights [1]. The effective manipulation or controlling of the polarization state

is always highly desirable due to its wide applications in wireless communications, liquid crystal display, optical data storage, and so on [2, 3]. The manipulation of the polarization is the ability to rotate or convert the polarization state of EM radiation as it reflects or transmits through a structure or media. The structure or media for polarization manipulation is mainly including polarizers, wave retarders, and polarization rotators. Conventionally, ferrite materials, grating structure, or levorotatory crystals based on birefringence effects have been proposed and utilized as wave plates for the polarization conversion. These wave plates require a relative long propagation distance to obtain enough phase accumulation, which usually suffers the energy loss and low efficiency problem, thus limiting some practical application. In the past decade, metamaterial (MM) as artificial media has been paid great attention and achieved much exotic functionality [4], such as negative refraction [5], superlens [6], EM cloak [7], perfect absorber [8]. The exotic EM properties mainly originate from the subwavelength unit cell structure of the MM rather than the intrinsic material properties, and the response strength and spectrum of the EM waves or lights can be regulated by changing microstructure, such as shape, size, and array formation of MMs [4]. Thus, how to realize the effective control and manipulation of polarization state through the MMs design has become a new research topic [9–14].

Generally, there are two kinds of design schemes of MMs for manipulating polarizations of lights. The first one is chiral metamaterial (CMM) [15], which usually operate well in transmission mode for manipulate polarization [16–23]. Another one is anisotropic MMs, which manipulates polarization in both transmission and reflection modes [11, 13, 24–27]. Compared with the conventional material or structure, those MMs-based polarization rotators or converters have some advantages, such as thin

✉ Yongzhi Cheng
cyz0715@126.com; chengyz@wust.edu.cn

¹ School of Electronics and Information Engineering, Beihang University, Beijing 100191, China

² School of Information Science and Engineering, Wuhan University of Science and Technology, Wuhan 430081, Hubei, China

thickness, weight-light and also can be scaled to other EM spectrum due to the geometry scalability. However, the bandwidth and efficient are still main concerns that need improvement. There are mainly two methods to broaden the bandwidth, one of which is stacking metallic–dielectric multilayers [28–30]. The other method is using anisotropic high-impedance surfaces, and the operating frequency band can be broadened by multiple plasmon resonances [24–27, 31, 32]. However, for the previous most converters or rotators operated in the reflection mode, the undesirable high co-polarization reflection severely limits the efficiency and the operation bandwidth. To extend the functionality, the reflective polarization rotators with broadband and high efficient are highly desirable [26].

Here, we present design, fabrication, and characterization of a high-efficiency and broadband reflective 90° linear polarization rotator based on anisotropic MM at microwave frequencies. This designed anisotropic MM comprises an array of combination of disk and split-ring resonator (named as DSRR), which is demonstrated by simulation and experiment for both y - and x -polarization rotation. Moreover, the proposed anisotropic MM still performs well in the operation band for oblique incident waves, providing convenience in practical applications. An underlying physical mechanism is investigated through the decomposed electric field components that interact with the DSRRs and the simulated surface current distribution.

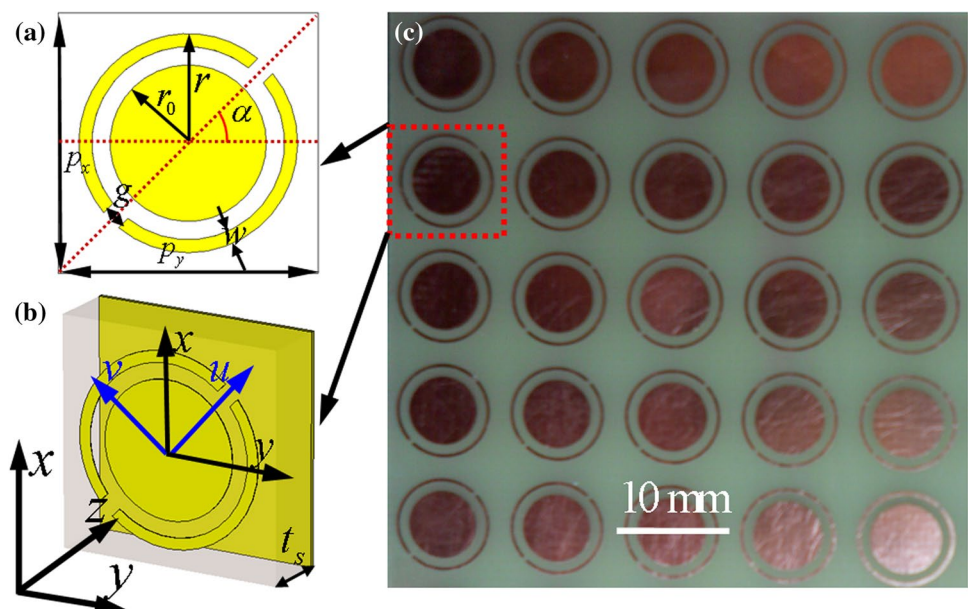
2 Design, simulation, and measurement

The proposed anisotropic MM for the reflective polarization rotation is consisting of an intermediate dielectric

layer sandwiched with a top DSRR and a bottom continuous metallic layer, as shown in Fig. 1a, b. It is benefit for polarization manipulation in reflection mode. The DSRR has a symmetric axis marked by $u(v)$ -axis along 45° direction respect to x - or y -axis as shown in Fig. 1b. Therefore, the proposed structure can be regarded as an anisotropic homogeneous MM with dispersive relative permittivity and permeability. When a plane wave with a prescribed polarization illuminates the DSRR surface, both x - and y -polarized reflected and transmitted waves are generated due to the anisotropic characteristics of the designed MM [32]. The DSRR orientation is such that incident waves with the polarization along the x - or y -axis are rotated by 90° to their orthogonal polarization state after reflecting off the structure. We can analyze reflective polarization conversion using u , v , and z as the orthogonal coordinate system. The optimal geometric parameters of the unit cell structure are as following: $p_x = p_y = 10$ mm, $r_0 = 3$ mm, $r = 4.2$ mm, $w = 0.5$ mm, $g = 0.8$ mm, $t_s = 2.9$ mm, $\alpha = 45^\circ$. Thus, the structure can be avoided diffraction at the normal incidence for frequencies up to 30 GHz.

In order to study its efficiency and gain insight into the mechanism of the polarization rotation property of the designed anisotropic MM, numerical simulations were performed using the CST Microwave Studio based on a finite integration method. The periodic boundary conditions are applied to the x and y directions, and the absorbing boundary conditions are applied to the z direction. In simulation, we select the FR-4 board as an intermediate dielectric layer, and the relative dielectric constant is $\epsilon_r = 4.3(1 + i0.025)$. The $30\text{-}\mu\text{m}$ -thick copper film with an electric conductivity of $\sigma = 5.8 \times 10^7 \text{ s m}^{-1}$ is used as the metallic parts.

Fig. 1 Reflective linear polarization rotator based on DSRRs anisotropic metamaterial: **a** front view of the unit cell, **b** perspective view of the unit cell, while u - and v -axes are used to mark the structure anisotropic axes. **c** The portion photograph of the tested sample



To experimentally demonstrate the proposed polarization rotator, the design shown in Fig. 1b has been fabricated with traditional print circuit board (PCB) technology. The geometric parameters of the unit cell structure in fabrication are the same with the ones in simulation. In experiment, the front and back metallic layer is 30-μm-thick copper film, and the middle dielectric layer is the FR-4 substrate with 2.9 mm thickness, which are the same with simulation. Figure 1c shows the portion photographs of the samples with an overall size of 200 × 200 mm² including 20 × 20 unit cells. The measurements were carried out in an anechoic chamber. A vector network analyzer (Agilent N5244A) connected to the two standard gain horn antenna was used to measure the reflection coefficients of the fabricated sample. Incident plane waves with different linear polarizations could be generated by rotating the horn antennas with the horizontal z-axis. To better understand the polarization conversion of the anisotropic MM, we define $r_{xx} = |E_x^r/E_x^i|$, $r_{yx} = |E_y^r/E_x^i|$, $r_{xy} = |E_x^r/E_y^i|$ and $r_{yy} = |E_y^r/E_y^i|$ as the reflection coefficients in both simulation and experiment. Since the DSRR has the line symmetry when it rotating 45° along x or y direction, the co-polarization reflection coefficients of r_{xx} and r_{yy} and cross-polarization reflection coefficients r_{yx} and r_{xy} are equivalent, respectively. Thus, only one linear polarization state (x-polarized or y-polarized wave) needs to be considered for the incident waves in both simulation and experiment. Hence, we just consider the incident x-polarized wave and the corresponding reflection coefficients r_{xx} and r_{yx} .

3 Results and discussions

Figure 2a shows the simulated and experimental magnitudes of reflection coefficients (r_{xx} and r_{yx}) for normal incident x-polarized waves. It can be observed that the simulations are in good agreement with experiments except that there is a minor discrepancy for the resonance frequencies due to the fabrication precision and the finite size effects in the sample. From Fig. 2a, there exist three resonant dips for co-polarization reflection coefficients r_{xx} at $f_1 = 5.9$ GHz, $f_2 = 7.8$ GHz and $f_3 = 10.0$ GHz, and the curve of which shows three dip values that are below 0.1. In addition, from 5.7 to 10.3 GHz, the cross-polarization reflection coefficient r_{yx} is greater than 0.85, while the co-polarization reflection coefficient r_{xx} is below 0.3. It indicates that there is nearly no x-polarization component in reflected waves but only high reflection for cross-polarization around above frequency range. It means that nearly all energy of incident waves with x-polarization is converted to y-polarized ones after reflection.

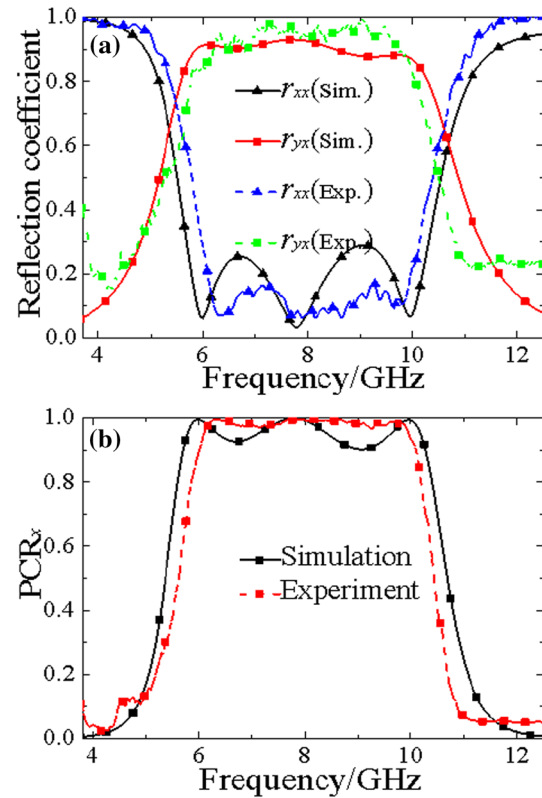


Fig. 2 Simulated and experimental results: **a** reflective coefficients of cross-polarization and co-polarization (r_{yx} and r_{xx}); **b** polarization conversion ratio (PCR_x)

To better demonstrate the polarization conversion by 90° rotation properties of the designed anisotropic MM, we define the polarization conversion ratio (PCR) as $PCR_x = |r_{yx}|^2 / (|r_{yx}|^2 + |r_{xx}|^2)$ for normal incident x-polarization wave [10]. Figure 2b shows the simulated and experimental PCR_x versus frequency. It is shown that the PCR_x is always above 0.9 in the frequency ranges from 5.7 to 10.3 GHz with a relative bandwidth of 57.5%. In addition, the PCR_x reaches near unity at above three resonance frequencies, meaning that nearly all energy of x-polarized incident wave is converted to y-polarized ones or rotated by 90°. The results demonstrate the capability of linear polarization rotation by 90° with high polarization purity over a broad bandwidth. Actually, this broad bandwidth enhancement operation results from the superposition of multiple polarization conversion peaks around 5.9, 7.8, and 10.0 GHz, which mainly benefits from the superposition of multiple resonance modes [28, 30]. It should be noticed that the performance will be influenced significantly by the sizing parameters of the unit cell structure of the designed anisotropic MM.

To gain insight into the broadband linear polarization rotation or conversion of the proposed structure, we have calculated ellipticity angle η and polarization rotation

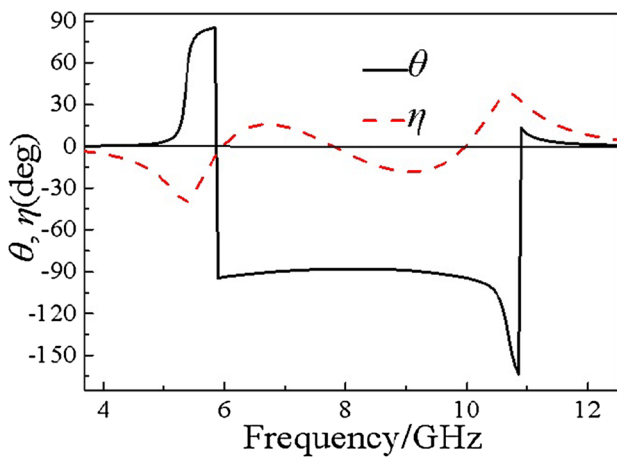


Fig. 3 Polarization azimuth rotation angle (θ) and polarization ellipticity angle (η)

azimuth angle θ for an incident x -polarized wave along the forward (+ z) direction by using the linear reflection coefficients, and they can be given as:

$$\eta = \frac{1}{2} \arcsin \left(\frac{2p_r \sin(\varphi_r)}{1 + |p_r|^2} \right), \tag{1}$$

$$\theta = \frac{1}{2} \arctan \left(\frac{2p_r \cos(\varphi_r)}{1 - |p_r|^2} \right), \tag{2}$$

where $p_r = |r_{yx}|/|r_{xx}|$ and $\varphi_r = \arg(r_{yx}) - \arg(r_{xx})$. The η describes the polarization state, and the θ denotes the polarization rotation angle of the reflected waves respected to the incident waves.

From Fig. 3, it can be observed that the absolute value of the η is close to zero at resonance frequency and is below 15° from 5.7 to 10.3 GHz, indicating that the reflected cross-polarization wave is near linear polarization with relative high polarization purity. We employ the polarization azimuth rotation angle θ to describe the angle between the major polarization axis and x -axis as shown in Fig. 3. We can see that the value of θ is near -90° from 5.7 to 10.3 GHz for incident x -polarized wave, indicating that the polarization plane of the reflected wave experiences near -90° rotation respect to the incident wave in this broadband range. It also means that when incident waves with x polarization (+ x direction) passing through the designed MM slab propagating along the forward (+ z) direction can nearly perfectly convert to reflected wave propagating along the backward ($-z$) direction with y polarization ($-y$ direction) in the frequency range of 5.7–10.3 GHz.

To get the polarization rotation properties of designed MM for oblique incidence, we also simulated the PCR_y and PCR_x under oblique incidence waves with the TE and TM polarizations. As shown in Fig. 4a, b, for both polarizations, around the lower and higher frequencies (5.9 and 10.0 GHz), the values

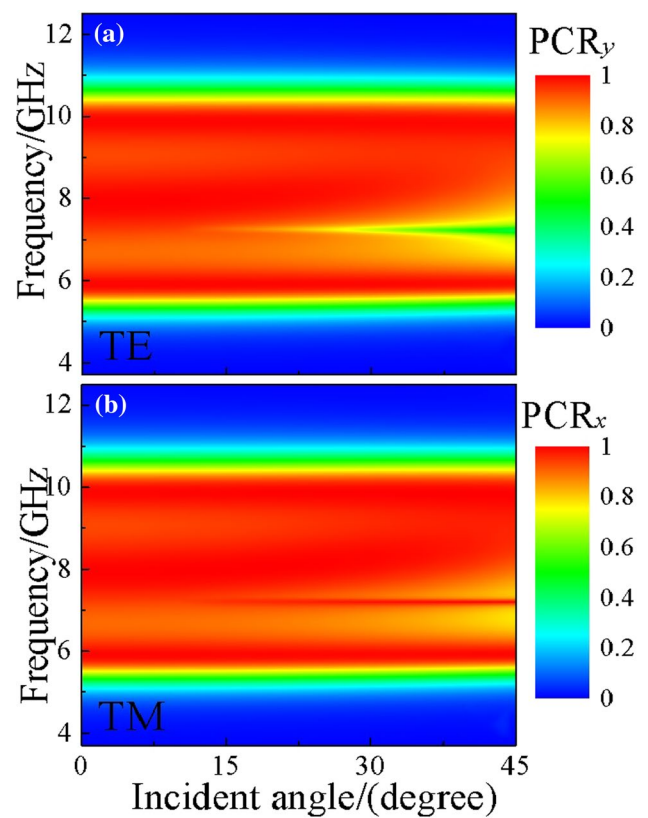


Fig. 4 PCR under the oblique incidence: **a** PCR_y for TE polarization, **b** PCR_x for TM polarization

of the PCR_y and PCR_x are nearly unchanged when increasing incident angle, indicating that the polarization rotation is nearly unaffected for the oblique incidence. In addition, around the frequency of 7.8 GHz, the value of PCR_y will decrease gradually with the increase in the incident angle, while the PCR_x is nearly unchanged. However, for both polarizations of TE and TM modes, values of the PCR_y and PCR_x are greater than 60 %, revealing that this broadband and high-efficient performance is sustained over a wide incidence angle range.

Taking a further step, to better understand the operational principles, we investigate the EM response of the anisotropic MM for normal incident waves. The polarization direction of the incident plane EM wave is along the x -axis, which can be decomposed into two perpendicular components, u and v , as shown inset of Fig. 5a. The electric field E_i of the incident wave at first interface plane can be described as $E_i = (E_{iu}u + E_{iv}v)e^{i(-kz+\omega t)}$, and electric field of the reflected wave can be expressed as $E_r = (r_u E_{iu}u + r_v E_{iv}v)e^{i(kz+\omega t)}$, where $r_{u(v)} = e^{\Delta\varphi_{u(v)}}$ is the reflection coefficient along the $u(v)$ -axis and $\Delta\varphi_{u(v)}$ is the phase change after reflection, respectively. Similar to the previous reported structures [30–32], the multiple plasmon resonances of MM will be excited by interacting with incident EM wave E_i . To detail analyze plasmon resonance

eigenmodes of MM unit cell, we performed simulation again by full-wave simulations.

Figure 5 shows the spectra of co-polarization reflection versus frequency under normal incidence with the

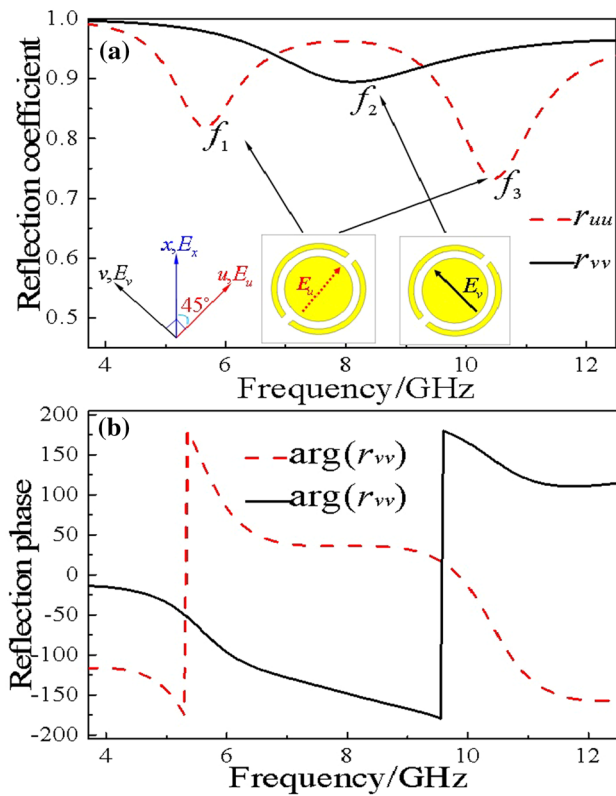
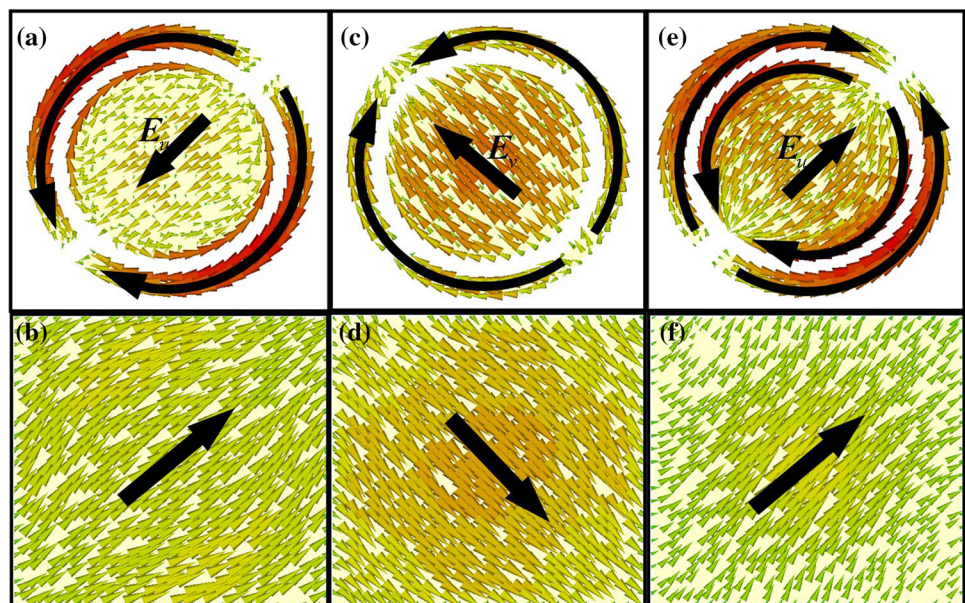


Fig. 5 Simulated co-polarization **a** reflective coefficients and **b** phases for v -polarized and u -polarized wave's incidence

polarization along u and v directions, respectively. As shown in Fig. 5a, it can be observed that there are all three dips for the co-polarization reflection, which predicts the presence of plasmon resonance eigenmodes in our designed anisotropic MM. At f_1 and f_3 , the eigenmodes are excited by v component of the electric field E_v , while at f_2 , the one is excited by the u component of the incident EM waves. Furthermore, as shown in Fig. 5b, the phase difference $\Delta\phi_{u(v)}$ of the reflected electric components E_{ru} and E_{rv} is close to $\pm 180^\circ$ at the resonance frequencies, which causes polarization rotation by 90° for the incident E_i with polarization along x direction.

To investigate the physical mechanism of the polarization rotation by 90° for the proposed MM, the surface current distributions on the top and bottom layers are simulated at resonance frequencies of $f_1 = 5.9$ GHz, $f_2 = 7.8$ GHz, and $f_3 = 10$ GHz, respectively. From Fig. 6, the “anti-symmetric” and “symmetric” modes are excited on the DSRRs. As shown in Fig. 6a, b, e, f, at frequencies of $f_1 = 5.9$ GHz and $f_3 = 10$ GHz, it can be observed that the unit cell structure only response to the E_u component of the incident x -polarized wave. While at $f_2 = 7.8$ GHz, the unit cell structure only response to the E_v component of the incident x -polarized wave, as shown in Fig. 6c, d. At $f_1 = 5.9$ GHz and $f_2 = 7.8$ GHz, the directions of the induced surface current at the top and bottom metallic layers are antiparallel, indicating “anti-symmetric” and a magnetic coupling resonance [33]. In these cases, the DSRRs can be regarded as a magnetic dipole. At $f_3 = 10$ GHz, the flow directions of the induced surface current at the top and bottom metallic layers are the same, indicating “symmetric” and an electric coupling resonance. Hence, in this case, the DSRRs can be regarded as an electric dipole. Thus,

Fig. 6 Surface current distributions on the DSRRs (a, c, e) and metallic ground plane (b, d, f) of the unit cell of the designed anisotropic MM under the normal incident x -polarized waves at three resonant frequencies: **a, b** $f_1 = 5.9$ GHz, **c, d** $f_2 = 7.8$ GHz, **e, f** $f_3 = 10$ GHz



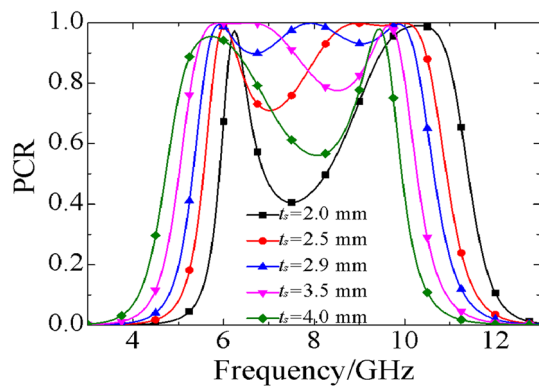


Fig. 7 Simulated PCR for different thickness of the dielectric substrate

the polarization rotator can work in broadband due to the superposition of multiple magnetic and electric resonance responses characteristic.

We also study the influence of the geometric parameter to the performance of the proposed polarization rotator. We can expect that the bandwidth and PCR will be influenced significantly by changing the sizing parameters of the unit cell structure of the designed anisotropic MM. In particular, the PCR will be deteriorated if fixed the period (p_x and p_y) of anisotropic MM when just changing the other geometric parameters. For example, as shown in Fig. 7, the simulation results indicate that the thickness of the dielectric substrate will influence significantly the bandwidth and magnitude of the PCR. From Fig. 7, it is clear that the operation frequency is decreased gradually, and the relative bandwidth is nearly unchanged as the substrate thickness increases. However, when the dielectric substrate is become thicker or thinner than a certain value, the performance of the MM becomes worse. Thus, the performance and bandwidth should be taken into consideration when designing the polarization rotator.

4 Conclusion

In conclusion, a high-efficiency and broadband reflective 90° linear polarization rotator based on anisotropic MM is proposed and demonstrated by both simulation and experiment. The anisotropic MM is composed of periodic array of DSRR structure placed over a ground plane. Simulation results exhibit that high-efficiency and broadband cross-polarization reflection and low co-polarization reflection are achieved from 5.7 to 10.3 GHz with a mean polarization conversion ratio of 90 %, which agrees well with experiments. Furthermore, the proposed rotator can maintain the high performance over a wide incidence angle range for both y - and x -polarized wave.

Such MM-based polarization rotation has great application values in the polarization-controlled devices, stealth surfaces, antennas, etc.

Acknowledgments This work is supported by the National Natural Science Foundation of China (NSFC) (Grant No. 61605147) and the Youth science and technology backbone cultivation plan project of the Wuhan University of Science and Technology (Grant No. 2016xz010).

References

1. H. Eugene, *Optics* (Addison Wesley, New York, 2002), p. 78
2. J. Lub, P. van de Witte, C. Doornkamp, J.P.A. Vogels, R.T. Wegh, *Adv. Mater.* **15**, 1420 (2003)
3. M.R. Andrews, P.P. Mitra, R. de Carvalho, *Nature* **409**, 316 (2001)
4. T.J. Cui, R.S. David, R. Liu, *Metamaterials: Theory, Design, and Applications* (Springer, New York, 2010), p. 9
5. Z.Z. Cheng, Y.Z. Cheng, *Microw. Opt. Technol. Lett.* **53**, 615 (2011)
6. I.I. Smolyaninov, Y.J. Hung, C.C. Davis, *Science* **315**, 1699 (2007)
7. D. Schurig, J.J. Mock, B.J. Justice et al., *Science* **314**, 977 (2006)
8. Y.Z. Cheng, T. Xiao, H.L. Yang, B.X. Xiao, *Acta Phys. Sin.* **59**, 5715 (2010)
9. A.V. Rogacheva, V.A. Fedotov, A.S. Schwanecke, N.I. Zheludev, *Phys. Rev. Lett.* **97**, 177401 (2006)
10. J. Hao, Y. Yuan, L. Ran et al., *Phys. Rev. Lett.* **99**, 063908 (2007)
11. J.Y. Chin, M. Lu, T.J. Cui, *Appl. Phys. Lett.* **93**, 251903 (2008)
12. Y.Q. Ye, S.L. He, *Appl. Phys. Lett.* **96**, 203501 (2010)
13. W.J. Sun, Q. He, J.M. Hao, L. Zhou, *Opt. Lett.* **36**, 927 (2011)
14. L.T. Chen, Y.Z. Cheng, Y. Nie, R.Z. Gong, *Acta Phys. Sin.* **61**, 094203 (2012)
15. Z. Li, M. Mutlu, E. Ozbay, *J. Opt.* **15**, 023001 (2013)
16. Y. Cheng, Y. Nie, X. Wang, R. Gong, *Appl. Phys. A* **111**, 209 (2013)
17. C. Huang, Y. Feng, J. Zhao, Z. Wang, T. Jiang, *Phys. Rev. B* **85**, 195131 (2012)
18. J.K. Gansel, M. Thiel, M.S. Rill, M. Decker, K. Bade, V. Saile, G. Freymann, S. Linden, M. Wegener, *Science* **325**, 1513 (2009)
19. H.X. Xu, G.M. Wang, M.Q. Qi, T. Cai, *Prog. Electromagn. Res.* **143**, 243 (2013)
20. Y.Z. Cheng, R.Z. Gong, Z.Z. Cheng, Y. Nie, *Appl. Opt.* **53**, 5763 (2014)
21. M. Decker, R. Zhao, C.M. Soukoulis, S. Linden, M. Wegener, *Opt. Lett.* **35**, 1593 (2010)
22. M.H. Li, L.Y. Guo, H.L. Yang, *Microw. Opt. Technol. Lett.* **56**, 2381 (2014)
23. Y.Z. Cheng, C.J. Wu, Z.Z. Cheng, R.Z. Gong, *Prog. Electromagn. Res.* **155**, 105 (2016)
24. M. Feng, J. Wang, H. Ma, W. Mo, H. Ye, S. Qu, *J. Appl. Phys.* **114**, 074508 (2013)
25. Y.Z. Cheng, W. Withayachumnankul, A. Upadhyay, D. Headland, Y. Nie, R.Z. Gong, M. Bhaskaran, S. Sriram, D. Abbott, *Appl. Phys. Lett.* **105**, 181111 (2014)
26. L. Zhang, P. Zhou, H. Lu, H. Cheng, J. Xie, L. Deng, *IEEE Antennas Wirel. Propag. Lett.* **14**, 1157 (2015)
27. Z.Y. Wei, Y. Cao, X.Yu. Fan, H. Li, *Appl. Phys. Lett.* **99**, 221907 (2011)
28. Y.Z. Cheng, Y. Nie, Z.Z. Cheng, L. Wu, X. Wang, R.Z. Gong, *J. Electromagn. Waves Appl.* **27**, 1850 (2013)
29. X.J. Huang, B.X. Xiao, D. Yang, H.L. Yang, *Opt. Commun.* **338**, 416 (2015)

30. N.K. Grady, J.E. Heyes, D.R. Chowdhury, Y. Zeng, M.T. Reiten, A.K. Azad, A.J. Taylor, D.A. Dalvit, H.T. Chen, *Science* **340**, 1304 (2013)
31. X. Gao, X. Han, W.P. Cao, H.O. Li, H.F. Ma, T.J. Cui, *IEEE Trans. Antennas Propag.* **63**, 3522 (2015)
32. H.Y. Chen, J.F. Wang, H. Ma, S.B. Qu, J.Q. Zhang, Z. Xu, A.X. Zhang, *Chin. Phys. B* **24**, 014201 (2015)
33. Y.Z. Cheng, Z.Z. Cheng, R.Z. Gong, *Opt. Commun.* **361**, 41 (2016)